UCRL-PROC-232219

LAWRENCE
LIVERMORE
NATIONAL
LABORATORY

Turbulence and transport during electron cyclotron heating in the DIII-D tokamak

T. L. Rhodes, W. A. Peebles, J. C. DeBoo, R. Prater, J. E. Kinsey, J. S. deGrassie, R. V. Bravenec, K. H. Burrell, J. Lohr, C. C. Petty, X. V. Nguyen, E. J. Doyle, C. M. Greenfield, L. Zeng, M. A. Zeeland, G. Wang, M. A. Makowski, G. M. Staebler, H. E. St. John, W. M. Solomon

June 27, 2007

34th EPS Conference on Plasma Physics
Warsaw, Poland
July 2, 2007 through July 6, 2007

Disclaimer

This document was prepared as an account of work sponsored by an agency of the United States Government. Neither the United States Government nor the University of California nor any of their employees, makes any warranty, express or implied, or assumes any legal liability or responsibility for the accuracy, completeness, or usefulness of any information, apparatus, product, or process disclosed, or represents that its use would not infringe privately owned rights. Reference herein to any specific commercial product, process, or service by trade name, trademark, manufacturer, or otherwise, does not necessarily constitute or imply its endorsement, recommendation, or favoring by the United States Government or the University of California. The views and opinions of authors expressed herein do not necessarily state or reflect those of the United States Government or the University of California, and shall not be used for advertising or product endorsement purposes.

Turbulence and transport during electron cyclotron heating in the DIII-D tokamak

T.L. Rhodes,[a)] W.A. Peebles,[a)] J.C. DeBoo,[b)] R. Prater,[b)] J.E. Kinsey,[b)] J.S. deGrassie,[b)] R.V. Bravenec,[c)] K.H. Burrell,[b)] J. Lohr,[b)] C.C. Petty,[b)] X.V. Nguyen,[a)] E.J. Doyle,[a)] C.M. Greenfield,[b)] L. Zeng,[a)] M.A. Van Zeeland,[b)] G. Wang,[a)] M.A. Makowski,[d)] G.M. Staebler,[b)] H.E. St John,[b)] and W.M. Solomon[e)]

[a)]University of California-Los Angeles, Los Angeles, California, USA

[b)]General Atomics, P.O. Box 85608, San Diego, California 92186-5608, USA

[c)]University of Texas-Austin, Austin, Texas 78712, USA

[d)]Lawrence Livermore National Laboratory, Livermore, California 94550, USA

[e)]Princeton Plasma Physics Laboratory, Princeton, New Jersey 08543-0451, USA

(Received on

Abstract The response of plasma parameters and broad wavenumber turbulence (1–40 cm^{-1}, $k\rho_s$ = 0.1–8) to auxiliary electron cyclotron heating (ECH) is reported on. In these plasmas the electron temperature responds most strongly to the ECH while the electron density and ion temperature are kept approximately constant. Thermal fluxes and diffusivities increase appreciably with ECH for both electron and ion channels. Significant changes to the density fluctuations over the full range of measured wavenumbers are observed. This range of wavenumbers encompasses that typically associated with ion temperature gradient, trapped electron mode, and electron temperature gradient modes. Changes in linear growth rates calculated using a gyrokinetic code show consistency with observed fluctuation increases over the whole range of wavenumbers.

PAC Nos.

1. Introduction

Anomalous electron heat transport is an important and unresolved issue that directly impacts the understanding and prediction of fusion reactor performance [1,2]. Although lower wavenumber turbulence and resulting transport are thought to be fairly well understood [1,2], the interaction of low, intermediate, and high-k fluctuations and their combined impact on transport is a potentially complex system that calls for measurements over a broad wavenumber range [3-5]. Turbulence measurements over a range in wavenumbers have been undertaken on a variety of fusion research devices including DIII-D [the results reported here and references 6,7], FT-2 [8,9], Tore-Supra [10], and NSTX [11]. These efforts generally employ some type of scattering to access the wavenumber range of interest, from forward far infrared (FIR) and mm-wave backscattering [DIII-D, reference 6], enhanced upper-hybrid resonance backscattering [FT-2, reference 8], far-forward FIR scattering [Tore-Supra, reference 10], to forward FIR scattering [NSTX, reference 9]. These experiments have found fluctuations over a large range in wavenumber corresponding to the wavenumber ranges of low-k ion temperature gradient instability (ITG), trapped electron mode (TEM), up to and including high-k electron temperature gradient instability (ETG). The question of how much transport can be attributed to high-k, ETG type modes is currently an unresolved question. Since these modes can interact with, and perhaps be driven by, the lower k fluctuations it is important to measure the turbulence over as broad a range as possible. In this regard, work on DIII-D indicates that the high k ETG scale fluctuations can evolve independently of lower k fluctuations in some cases [7]. However, many more plasma regimes, parameters, wavenumbers, radial locations, etc. as well as utilization of different

research devices are thought necessary before a firm understanding of these higher k fluctuations is achieved.

In this paper the effects of electron cyclotron heating (ECH) upon Ohmic discharges are examined from the point view of plasma parameters, turbulence, and transport. Turbulence measurements over a broad range in wavenumber (1–40 cm^{-1}, $k\rho_s$ = 0.1–8) from multiple scattering diagnostics are presented. The measurements cover this wavenumber range with a significantly higher number of wavenumber points than previously reported on DIII-D due to upgraded and new diagnostic systems. In general, the density turbulence increases in level with ECH over the range of wavenumbers studied. The plasma parameter most affected by the ECH is the electron temperature, with the electron density and ion temperature roughly unchanged. Various stability parameters (e.g. a/L_n, a/L_{Te}, a/L_{Ti}) are found to vary with ECH. Gyrokinetic stability calculations using the GKS code [12] are performed using the measured plasma parameters. Some consistency between increase in measured fluctuation levels and increased calculated linear growth rates from GKS is found over the wavenumber range studied. The plasmas examined here have some similarities to the plasmas described in the first part of reference [7] but also some significant differences. Both are principally Ohmic plasmas with auxiliary ECH heating, however the power levels differ by a factor of ~1.7 and the density changes significantly in [7] with ECH. Other, more quantitative, differences will be discussed later. It is nevertheless found that there is significant congruence in the resulting measurements and interpretation for the two different plasma conditions.

2. Experimental Results

The experiments described here were performed on a lower single-null, diverted DIII-D discharge, with plasma parameters B_T = 2.1 T, I_p = 0.75 MA, n_{chord} = 1.8×10^{19} m^{-2}, and deuterium working gas. A moderate amount of 110 GHz ECH (1.4 MW) was applied to these Ohmic discharges during the plasma current flat top (figure 1). The heating location was located near normalized radial location $\rho \approx 0.6$, with a heating deposition width of approximately ±0.1 in normalized radial units. The density was well controlled during this time period by feedback control of the gas puff using the CO_2 interferometer signal (figure 1). Short duration neutral beam blips (10 ms) were injected at different times on repeat shots to obtain ion temperature and density information from charge exchange recombination (CER). The major change to the plasma due to the ECH was an increase in the electron temperature (figure 1). The analysis presented here focuses on two times during these discharges, the Ohmic time period at 1800 ms and the ECH time period at 3465 ms. Based upon the time histories of the various plasma parameters these times appear quite stationary. The plasmas examined here have some similarities to the plasma described in the first part of reference [7] but also some striking differences. The similarities being both are principally Ohmic plasmas with auxiliary ECH heating. The major qualitative differences are lower ECH power for the plasmas herein (~1.4 MW compared to ~2.4 MW in [7]) and the operational difference that the plasma density was allowed to decrease in [7] whereas it was kept relatively constant here [e.g. figure 1(a)]. Other, more quantitative, differences will be discussed later. In addition to these differences a much improved fluctuation data set was obtained for the plasmas reported upon here. This improved fluctuation data set consists

of a larger number of monitored wavenumbers enabled by upgraded and new diagnostic systems.

Profiles of electron and ion temperatures, electron density, and magnetic safety factor q for the two times of interest are shown in figure 2. The electron temperature is obtained from a combination of multipoint Thomson scattering and electron cyclotron emission and shows the largest change due to the ECH. Note that although the ECH is applied at normalized radial location $\rho = 0.6$ the electron temperature increases significantly inside of this location indicating an inward thermal transport. This phenomenon has been previously reported upon in various machines [13-16] and was concluded to be inconsistent with purely diffusive transport. The error bars shown are from multiple automatic spline fits to the data and indicate the one sigma error bar from the resulting distribution. For each fit the data are randomly varied within the measurement error and the profile refitted. The ion temperature is obtained from charge exchange recombination measuring the fully stripped carbon impurity. Electron density is obtained from a combination of Thomson scattering and density profile reflectometry. The magnetic safety factor q is obtained using the magnetic equilibrium code EFIT [17] constrained by motional Stark effect (MSE) measurements of the on-axis magnetic field [18]. The parameters (other than T_e) show little variation with the possible exception of the electron density at the edge that does show a small increase with ECH. In contrast to this, the inverse scale lengths (a/L_n, a/L_{Te}, a/L_{Ti}) do vary with the addition of ECH with the largest changes in a/L_{Te} being found in the deep core while a/L_n, and a/L_{Ti} vary in both the edge and core. Here $a =$ 0.65 m is the minor radius of the plasma on the outboard midplane. The magnetic safety factor q and the magnetic shear $\hat{s} = (r/q)(\partial q/\partial r)$

do not vary significantly with ECH [figure 2(d,h)]. Z_{eff} is approximately constant in radius with a value of 1.25±0.1 (calculated from charge balance using the measured electron density and the fully stripped carbon impurity density from CER) and did not change appreciably with ECH. These parameters, as well as those derived directly from them (e.g. $T_{\mathrm{e}}/T_{\mathrm{i}}$, collisionality, etc.) enter directly into stability calculations of the various modes believed responsible for anomalous plasma transport (e.g. ITG, ETG, TEM) [12,19-21].

The radial electric field E_{r} and its radial shearing rate $\gamma_{\mathrm{E\times B}}$ at these two times is shown in figure 3. The radial electric field is determined from the force balance equation using CER measurements of the fully stripped carbon temperature, density, and vertical and tangential velocities [22]. The radial electric field E_{r} and its radial shearing rate $\gamma_{\mathrm{E\times B}}$ do appear to decrease on average with the application of ECH. However, within the uncertainties there is no clear difference between the two times of interest. Additionally, the magnitude of the shearing rate $\gamma_{\mathrm{E\times B}}$ is quite low at both times (especially in relation to the growth rates of the various plasma instabilities as will be seen later).

Thermal fluxes and diffusivities were calculated by the ONETWO transport code [23] using the measured profiles (figure 2) and the ECH power deposition location ($r/a \sim 0.6$) for both ions and electrons. Thermal diffusivities are of interest as they indicate how fast the plasma transports thermal energy whereas thermal fluxes are of interest since they are most directly related to the turbulent fluxes through standard flux relations, e.g. the turbulence induced diffusive heat flux $\tilde{q}_{\mathrm{e}} = n\langle \tilde{T}_{\mathrm{e}} \tilde{E}_{\theta} \rangle / B \propto n k_{\theta} T_{\mathrm{e}}^{2} (\tilde{n}/n)^{2} / B$. Two different times are shown in figure 4 corresponding to no ECH (t = 1800 ms) and 1.4 MW of ECH

power (t = 3465 ms). Both the ion and electron thermal fluxes and diffusivities increase with ECH. The increase in the electron channel is most noticeable since there is a large increase for $r/a > 0$ and a *decrease* for $r/a < 0.6$. This decrease is a manifestation of the phenomenon discussed earlier (and reported in [13]) where although the ECH is deposited locally at $r/a \sim$ 0.6±0.1, the electron temperature increases interior to that, even though the temperature gradient is negative in that region (i.e. the diffusive transport should be down gradient). Since the ion temperature did not increase significantly the increase in the ion thermal flux may be consistent with an increased fluctuation driven flux due to increased fluctuation levels (see below). The picture for the electron thermal flux is more complicated. The strong increase in electron temperature [figure 2(a)] can account for much of the increase in $\tilde{q}_{\mathrm{e}} = n\langle \tilde{T}_{\mathrm{e}} \tilde{E}_{\theta} \rangle / B \propto n k_{\theta} T_{\mathrm{e}}^{2} (\tilde{n}/n)^{2} / B$, but not all. This is because the maximum increase in T_{e}^{2} is ~4 compared to a maximum increase in electron heat flux of ~6 [figure 4(b)]. Again one potential explanation is an increase in fluctuation driven transport due to increased fluctuation levels (over all wavenumber ranges). The electron and ion thermal diffusivities are shown in figure 4(b). Both are seen to increase with ECH. At all times the ion diffusivities are well above the neo-classical ion diffusivities. The Ohmic electron diffusivity is significantly below the ion diffusivity except near the edge. In contrast, the electron diffusivity during ECH approaches the ion values indicating a significant change in transport character.

The response of the turbulent density fluctuations was measured over a broad wavenumber range using a combination of FIR scattering and mm-wave backscattering diagnostics [6]. FIR scattering was utilized to monitor the wavenumber ranges 1 cm^{-1}

[figure 5(a)] and 8–15 cm^{-1} [figure 5(b-d)]. A scan of the intermediate wavenumber range 8–15 cm^{-1} was obtained by scanning the receive angle (proportional to the detected wavenumber) on reproducible shots. The FIR scattering diagnostic is aligned along the tokamak midplane and principally detects fluctuations with a poloidal wavenumber in the region near the midplane. The instrument function for these wavenumbers is quite broad in real space being approximately the full diameter of the plasma for 1 cm^{-1} and the minor radius for the 8–15 cm^{-1}. The FIR scattering system measures the fluctuations in the laboratory frame of reference, including both intrinsic fluctuation frequency and any $E \times B$ Doppler frequency shift that may be present [24,25]. The spatial variation of the combined intrinsic fluctuation frequency and the $E \times B$ Doppler frequency shift has been utilized to improve the spatial resolution of similar measurements [25]. In this picture higher measured frequencies are mapped to regions of larger total frequency that typically occur towards the mid-radius of the tokamak (the total frequency being the sum of the intrinsic fluctuation frequency and $E \times B$ Doppler frequency shift). This prescription gives rise to ambiguities since low frequencies can occur at both the edge and $r/a = 0$. This ambiguity is partially resolved by noting that fluctuation levels generally peak towards the edge. Thus, the edge region will tend to dominate the low frequency part of the power spectrum.

For the higher wavenumbers, $k \geq 20$ cm^{-1}, two channels of mm-wave backscattering are utilized. One channel detects ~20 cm^{-1} and integrates from the edge plasma inward to approximately $r/a = 0.2$ [figure 5(e)]. A second channel detects ~39 cm^{-1} and is spatially localized to the edge (r/a = 1.0±0.15) [figure 5(f)]. This spatial localization is accomplished by crossing a probe beam and a detection beam at an angle of ~12 deg. A

more complete description of the backscattering diagnostic can be found in [6,7]. These backscattering channels principally measure radial k and so are different from the FIR scattering in that respect. Two other channels of high-k at ~39 cm^{-1}, spatially localized to $r/=0.6$ and $r/a=0.35$, are available on these discharges however the plasma towards the edge is concentrated upon here.

For reference, the density wavenumber ranges in terms of normalized wavenumber, $k\rho_s$ (ρ_s is the ion gyroradius using the local electron temperature) are $k\rho_s \sim$ 0.1–0.2 for 1 cm^{-1}, $k\rho_s \sim$ 0.8–1.6 for 8.2 cm^{-1}, $k\rho_s \sim$ 1.2–2.4 for 12 cm^{-1}, $k\rho_s \sim$ 1.5–3.0 for 15 cm^{-1}, $k\rho_s \sim$ 2–4 for 20 cm^{-1}, $k\rho_s \sim$ 4–8 for 39 cm^{-1}. Here we have used values of the gyroradius (ρ_s = 0.1–0.2 cm) relevant to the outer region of these plasmas, $r/a > 0.7$. It is noted that ρ_s increases to values of ~0.3 cm at the core. This provides a total variation in $k\rho_s$ of 0.1–8 for the outer plasma region ($r/a =$ 0.7–1.0). This range in wavenumber is typically associated with ITG driven modes ($k\rho_s$ roughly 0.1–0.5), TEM ($k\rho_s \sim 0.5$ to 2 or greater), and ETG driven modes ($k\rho_s \sim 4$ and larger).

The fluctuation spectra shown in figure 5 are broad and generally featureless with the exception of the $k = 8.2$ and 12 cm^{-1} [figure 5(b,c)] data which show a rather wide low frequency peak. The frequency width of the spectra tends to increase with increasing wavenumber with the largest width (~1.5 MHz) occurring for the $k =$ 39 cm^{-1} data. These plasmas were relatively free of MHD type activity and this is reflected in the lack of coherent modes in the fluctuation data. In all cases the total fluctuation level $\tilde{n}$ (integrated over the individual frequency ranges shown) increases with ECH (the percentage change in $\tilde{n}$ is indicated in each figure). Note that this $\tilde{n}$ is not a normalized level (i.e. it is not $\tilde{n}/n$). The increase is not a constant change over each frequency range

but instead can be somewhat complicated. For example, the change in the $k = 12$ cm^{-1} data [figure 5(c)] occurs principally at low and high frequencies with the intermediate frequency range showing little variation. In contrast, the data for $k = 8.2$ cm^{-1} [figure 5(b)] shows an increase at the higher frequencies only. This variation with frequency is likely due to the spatial variation of the fluctuation level that is mapped onto frequency as discussed above. The more spatially localized channel [figure 5(f)] shows an increase at all frequencies up to the point that the instrument noise floor is reached.

As mentioned earlier, these plasmas show some similarity to those presented in the first part of reference [7] with some striking and important differences. The density and density profile were approximately constant here while they varied in [7]. The radial electric field and shear were both low and unchanged within error bars in contrast to the variation in E_r and, significantly, the increase in electric field shear reported in [7]. These differences are attributed to a combination of lower ECH power and, possibly more importantly, the relatively constant density that was obtained in these plasmas. The fluctuation data presented in this paper covers the same total range in wavenumber space but with a much larger number of monitored wavenumbers. The fluctuation levels are found to increase at all wavenumbers whereas those in [7] increased only at the highest k. There the lack of change at lower wavenumbers was attributed to the increase in electric field shear offsetting the increase in calculated growth rates [7]. It will be seen that the changes in fluctuation levels reported here are qualitatively consistent with the calculated growth rates for ITG–TEM–ETG type instabilities and, interestingly, are also consistent with the picture developed in [7].

3. Comparison with Linear Gyrokinetic Calculations

Comparisons of the above data to linear gyrokinetic simulations were performed using the GKS code [12]. GKS is a gyrokinetic stability code, which calculates linear growth rates and frequencies for toroidal drift waves corresponding to poloidal wavenumbers. Code inputs were the measured T_e, T_i, n_e, impurity profiles (assuming that the fully stripped carbon is the major impurity), and magnetic equilibrium (the profiles used are shown in figure 2). The effects due to up-down plasma asymmetries or $E \times B$ velocity shear flow (E and B are local electric and magnetic fields) are not included in GKS. Linear calculations do not simulate the fully developed turbulence but they can provide a guide as to where particular instabilities might appear. The GKS code calculates poloidal wavenumber characteristics, however the mm-wave backscatter data [$k = 20$ and 39 cm^{-1}, figure 5(e,f) respectively] are principally radial k (as contrasted with the FIR scattering which is principally k_θ). Nonlinear simulations of coupled ITG-TEM-ETG turbulence have recently shown isotropy in $k_r - k_\theta$ from $k\rho_s \sim 6$ to ~20 [4,5] approximately encompassing the experimental high k range reported here and indicating that such comparisons may be valid.

The results of the GKS simulations are summarized in figure 6, which shows growth rates and real frequencies versus radial location for a range of wavenumbers. The convention used in GKS is that positive growth rates indicate instability. Positive and negative frequencies correspond to propagation of the instability in the electron and ion diamagnetic drift directions respectively. The wavenumber ranges were chosen to encompass the experimental measurements shown in figure 5. The growth rates and frequencies are plotted in this manner to better show the variation with radial location as

well as with ECH. Examination of figure 6(a,b) shows that the linear growth rates respond in a somewhat complex manner, generally increasing towards the edge and decreasing or constant in the deep core. Note that the electric field shear shown in figure 3(b) is much lower than the calculated growth rates and so is not expected to significantly affect the fluctuations. Both the low and high k growth rates increase outside of $r/a \sim 0.8$, while tending to decrease interior to this. The increase outside of $r/a \sim 0.8$ is in qualitative agreement with the observed increase in fluctuation levels (figure 5) if the measured signals are assumed to arise principally from the outer regions. As discussed earlier the FIR scattering signals have been argued to be dominated by the high edge fluctuation levels consistent with this picture. The highest k signal, $k =$ 39 cm^{-1} [figure 5(f)], is spatially localized to the edge and so poses no interpretation issues in this regard. The $k =$ 20 cm^{-1} signal is less clear as it is a chord average from the edge into $r/a \sim 0.2$. However, if the fluctuations at this k peak towards the edge then there is reasonable agreement. The predicted increase in real frequency with increasing wavenumber [figure 6(c,d)] is in qualitative agreement with the increased spectral widths with increasing wavenumber shown in figure 5. It is interesting that the real frequencies at higher k [figure 6(d)] decrease in magnitude with ECH even though the growth rates increase. As mentioned earlier, GKS does not contain any effects of electric field or electric field shear and so the effects of shear must be evaluated separately. The small electric field and shearing rates of these plasmas (figure 3), and also the lack of variation in these in going from Ohmic to ECH thus greatly facilitates the comparisons with measurement. The increased electric field shear reported in [7] was conjectured to be the underlying cause of the lack of increase in measured lower k fluctuation levels as

compared to the predicted increase. The data presented here appear to be consistent with that picture since the fluctuations increase in a broadband manner similar to calculated growth rates while at the same time there is no strong variation in shear [it may in fact decrease, figure 3(b)].

Calculations of the critical gradient for ETG were performed using GKS. These showed that the outer plasma region ($r/a > 0.4$) of these discharges is unstable to ETG type modes, and that the difference between the experimental and critical gradients increases with ECH. This is indicative of a stronger level of ETG drive consistent with the measured increase at high k presented in figure 5(f). ITG type modes are predicted to be unstable by GKS towards the edge of these plasmas in the Ohmic case. With ECH this appears to change and an electron type mode, possibly TEM, appears.

4. Summary and Conclusions

In order to better understand plasma turbulence and the resulting transport selected plasmas were perturbed in a controlled manner while measuring a broad range of turbulence and plasma parameters. A data set suitable for comparison to theoretical predictions was an important goal and result of these experiments. Electron cyclotron heating was injected into a diverted, Ohmic DIII-D discharge and the plasma response measured. The density was well controlled and the resulting change to the gross plasma parameters was limited mainly to the electron temperature. The response of the density turbulence over a broad range in wavenumber (1–40 cm^{-1}, $k_{\perp}\rho_s$ = 0.1–8) was measured utilizing an increased number of higher wavenumber channels. The turbulence level increased significantly during ECH as did the thermal flux and diffusivity for both electron and ion channels. The observed fluctuation increases are consistent with changes in linear growth rates calculated using a gyrokinetic stability code over the whole range of wavenumbers if the fluctuation signals are assumed dominated by radii r/a greater than approximately 0.7. Experimentally, the changes in the ion and electron thermal fluxes require an increase in fluctuation levels similar to the measured increases. The electron thermal diffusivity increased to near the ion diffusivity levels during ECH.

From an operational point of view these types of plasma perturbations are quite useful as they result in changes to principally one parameter, in this case the electron temperature. The resulting changes in the various turbulence related stability parameters (e.g. a/L_n, a/L_{Te}, a/L_{Ti}, etc.) were more varied. In particular, the variation in a/L_{Ti} was larger than one would like. Nevertheless, by measuring the relevant parameters significant comparisons to theory and simulation can be performed. Future experiments

will seek to further separate and clarify the interactions and dependence between the low k and high k turbulence.

Acknowledgments

This work was performed under the auspices of the U. S. Department of Energy by University of California, Lawrence Livermore National Laboratory under Contrat W-7405-Eng-48.

References

[1] Carreras B A 1997 IEEE Trans. Plasma Sci. **25** 1281

[2] Horton W, 1999 Rev. Mod. Phys. **71**, 735

[3] Holland C and Diamond P H 2004 Phys. Plasmas **11** 1043

[4] Candy J and Waltz R E 2007 Fusion Energy 2006 (Proc. 21st Int. Conf. Chengdu, 2006) (Vienna: IAEA) CD-ROM file TH/2-1 and http://www-naweb.iaea.org/napc/physics/FEC/FEC2006/html/index.htm

[5] Waltz R E, Candy J and Fahey M 2007 Phys.Plasmas **14** 056116

[6] Rhodes T L, Peebles W A, Nguyen X V, Van Zeeland M A, deGrassie J S, Doyle E J, Wang G and Zeng L 2006 Rev. Sci. Instrum. **77** 10E922

[7] Rhodes T L, Peebles W A, Van Zeeland M A, deGrassie J S, Bravenec R V, Burrell K H, DeBoo J C, McKee G R, Lohr J, Petty C C, Nguyen X V, Doyle E J, Greenfield C M, Zeng L and Wang G 2007 Phys. Plasmas **14** 056117

[8] Gusakov E Z, Gurchenko A D, Altukhov A B, Stepanov A Yu, Esipov L A, Kantor M Yu and Kouprienko D V 2006 Plasma Phys. Control. Fusion **48** A371–A376

[9] Gusakov E Z, Gurchenko A D, Altukhov A B, Bulanin V V, Esipov L A, Kantor M Yu, Kouprienko D V, Lashkul S I, Petrov A V, Stepanov A Yu 2006 Fusion Energy 2006 (Proc. 21st Int. Conf. Chengdu, 2006) (Vienna: IAEA) CD-ROM file EX_P4-32 and http://www-naweb.iaea.org/napc/physics/FEC/FEC2006/html/index.htm

[10] Hennequin P, Sabot R, Honoré C, Hoang G T, Garbet X, Truc A, Fenzi C and Qéméneur A Q 2004 Plasma Phys. Control. Fusion **46** B121

[11] Kaye S M, Levinton F M, Stutman D, Tritz K, Yuh H, Bell M G, Bell R E, Horton W, Kim J, LeBlanc B P, Maingi R, Mazzucato E, Menard J E, Mikkelsen D, Park H, Rewoldt G, Sabbagh S A, Smith D R, Wang W and the NSTX Group 2006 Fusion Energy 2006 (Proc. 21st Int. Conf. Chengdu, 2006) (Vienna: IAEA) CD-ROM file EX-8-6 and http://www-naweb.iaea.org/napc/physics/FEC/FEC2006/html/index.htm

[12] Kotschenreuther M, Rewoldt G W and Tang W M, 1995 Comput. Phys. Commun. **88** 128

[13] Luce T C, Petty C C, de Haas J C M 1992 Phys. Rev. Lett. **68** 52

[14] Mantica P, Ryter F, Capuano C, Fahrbach H U, Leuterer F, Suttrop W, Weiland J 2006 Plasma Phys. Control. Fusion **48** 385

[15] Sozzi C *et al.* 2000 *18th IAEA Fusion Energy Conf. (Sorrento)* exp 5-13

[16] Mantica P *et al* 2000 Phys. Rev. Lett. **85** 4534

[17] Lao L L, St John H E, Peng Q, Ferron J R, Strait E J, Taylor T S 2005 Fusion Sci. Tech. **48** 968

[18] Holcomb C T et al. 2006 Rev. Sci. Instrum. **77** 10E506

[19] Weiland A, Jarmen B and Nordman H 1989 Nucl. Fusion **29** 1810

[20] Davydova T A, Weiland J and Yakimenko A I 2002 Phys. Plasmas **9** 4623

[21] Dong J Q, Horton W and Kim J Y 1992 Phys. Fluids B **4** 1867

[22] Burrell K H 1997 Phys. Plasmas **4** 1499

[23] St John H E, Taylor T S, Lin-Liu Y R and Turnbull A D 1994 Plasma Phys. Control. Nucl. Fusion Research **3** 603

[24] Koch R A and Tang W M 1978 Phys. Fluids **21** 1236

[25] Philipona R, Groebner R J, Burrell K H, Doyle E J, Gohil P, Luhmann, Jr. N C, Matsumoto H, Peebles W A, Rettig C L, and Stambaugh R D 1993 Phys. Fluids B **5** 87

List of Figure Captions

Figure 1. Time histories of (a) chord averaged electron density current from a CO_2 interferometer, (b) electron temperature from electron cyclotron emission from three radial positions, $\rho = 0.3$, $\rho = 0.4$ and $\rho = 0.6$, and (c) electron cyclotron heating power (heating location $\rho = 0.6$).

Figure 2. Profiles for two times: 1800 ms Ohmic (solid line) and 3465 ms ECH (dashed line). Representative uncertainties are indicated by the dotted lines. (a) Electron temperature from multipoint Thomson scattering and electron cyclotron emission, (b) ion temperature from charge exchange recombination spectroscopy, (c) electron density from multipoint Thomson scattering and profile reflectometry, and (d) magnetic safety factor q from magnetic equilbrium reconstruction code EFIT. The corresponding inverse scale lengths scaled by the minor radius a are shown in (e) through (g), (h) is the magnetic shear $\hat{s} = (r/q)(\partial q/\partial r)$.

Figure 3. (a) Radial electric field and its (b) shearing rate for the two times: 1800 ms Ohmic (solid line) and 3465 ms ECH (dashed line). Representative uncertainties are indicated by the dotted lines.

Figure 4. Electron and ion (a) thermal fluxes and (b) diffusivities for the two times: 1800 ms Ohmic and 3465 ms ECH. The neo-classical ion diffusivities are shown in (b) for reference.

Figure 5. Power spectra ($\tilde{n}^2$) for (a) k = 1 cm^{-1}, (b) k = 8.2 cm^{-1}, (c) k = 12 cm^{-1}, (d) k = 15 cm^{-1}, (e) k = 20 cm^{-1}, and (f) k = 39 cm^{-1} for the two times: 1800 ms Ohmic (black) and 3465 ms ECH (red). The change in the integrated fluctuation levels relative to the Ohmic time is indicated for each wavenumber. The range of integration is the range shown in each figure.

Figure 6. GKS calculations of linear growth rates for (a) $k_\theta\rho_s$ = 0.1–1 and (b) $k_\theta\rho_s$ = 2–10 for the Ohmic and ECH times. The upper and lower bounds of each area generally corresponds to the upper and lower range of $k_\theta\rho_s$ used. The matching real frequencies are shown in (c) and (d).

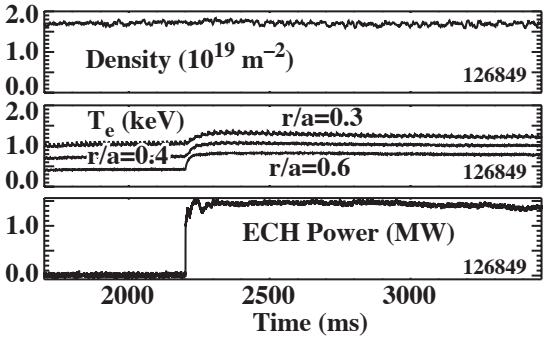

T.L. Rhodes Figure 1

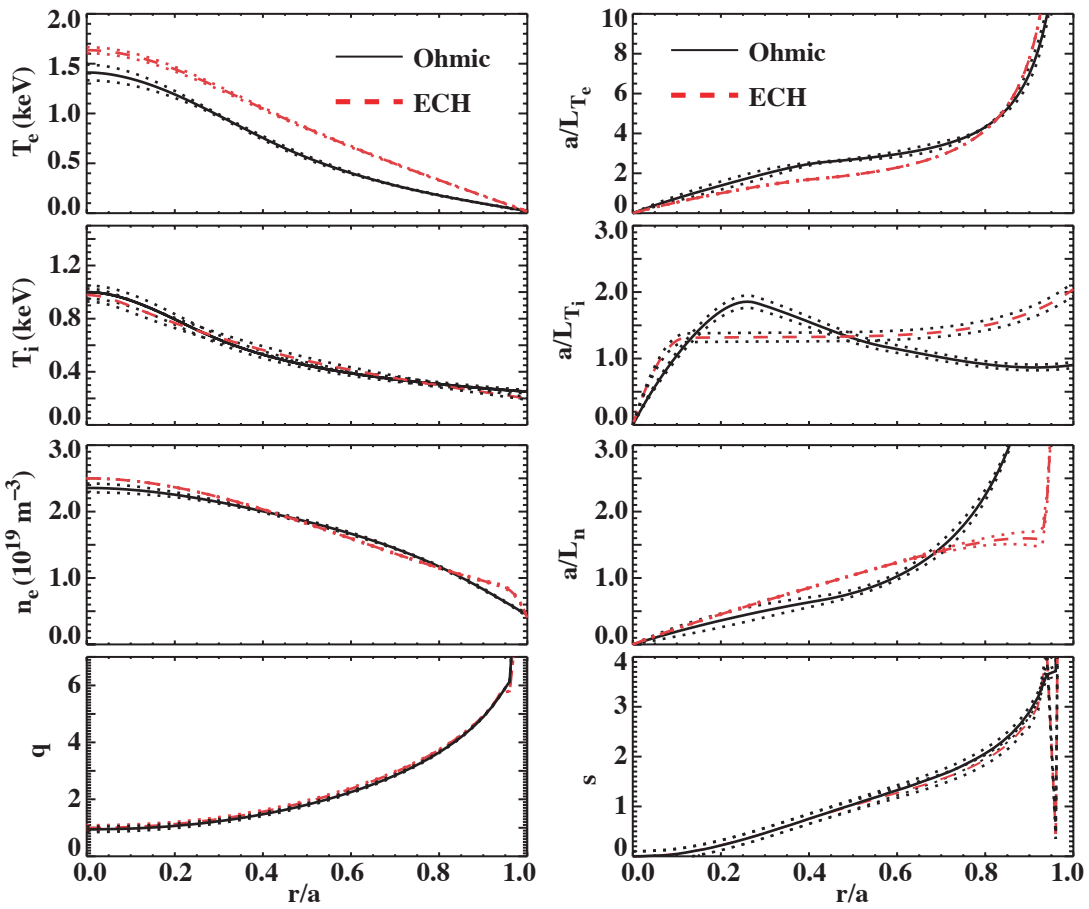

T.L. Rhodes Figure 2

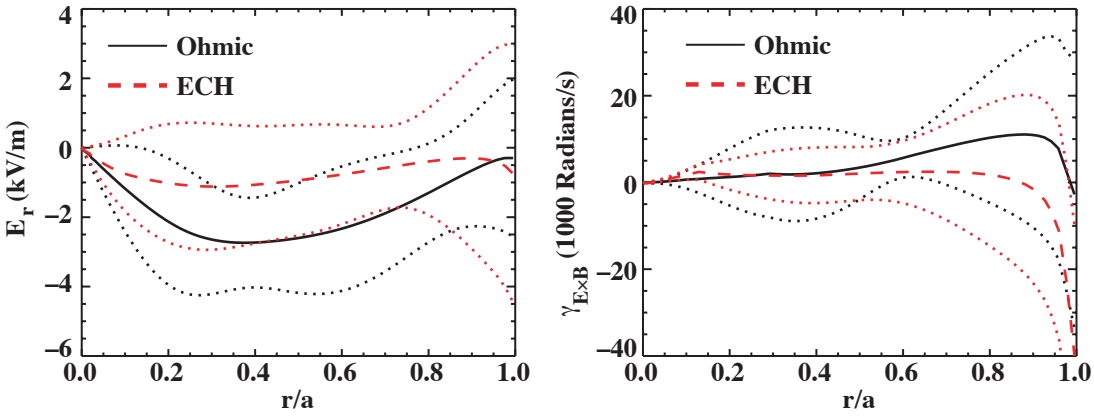

T.L. Rhodes Figure 3

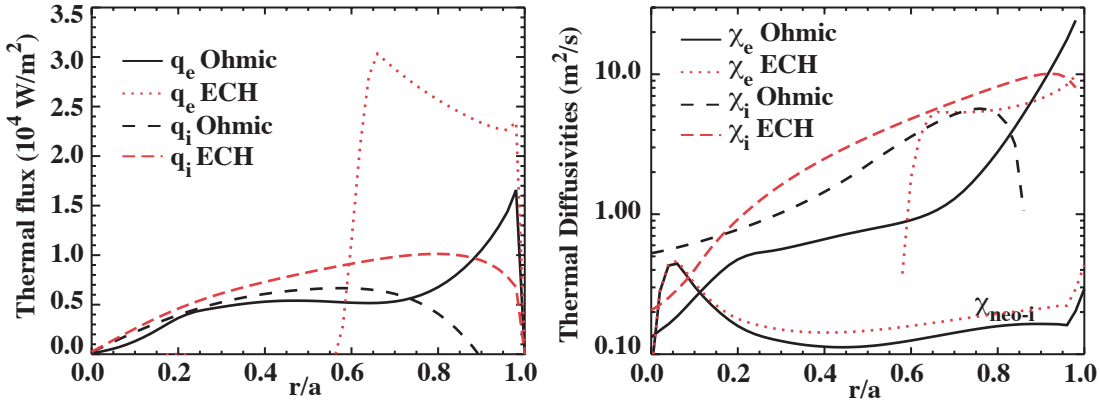

T.L. Rhodes Figure 4

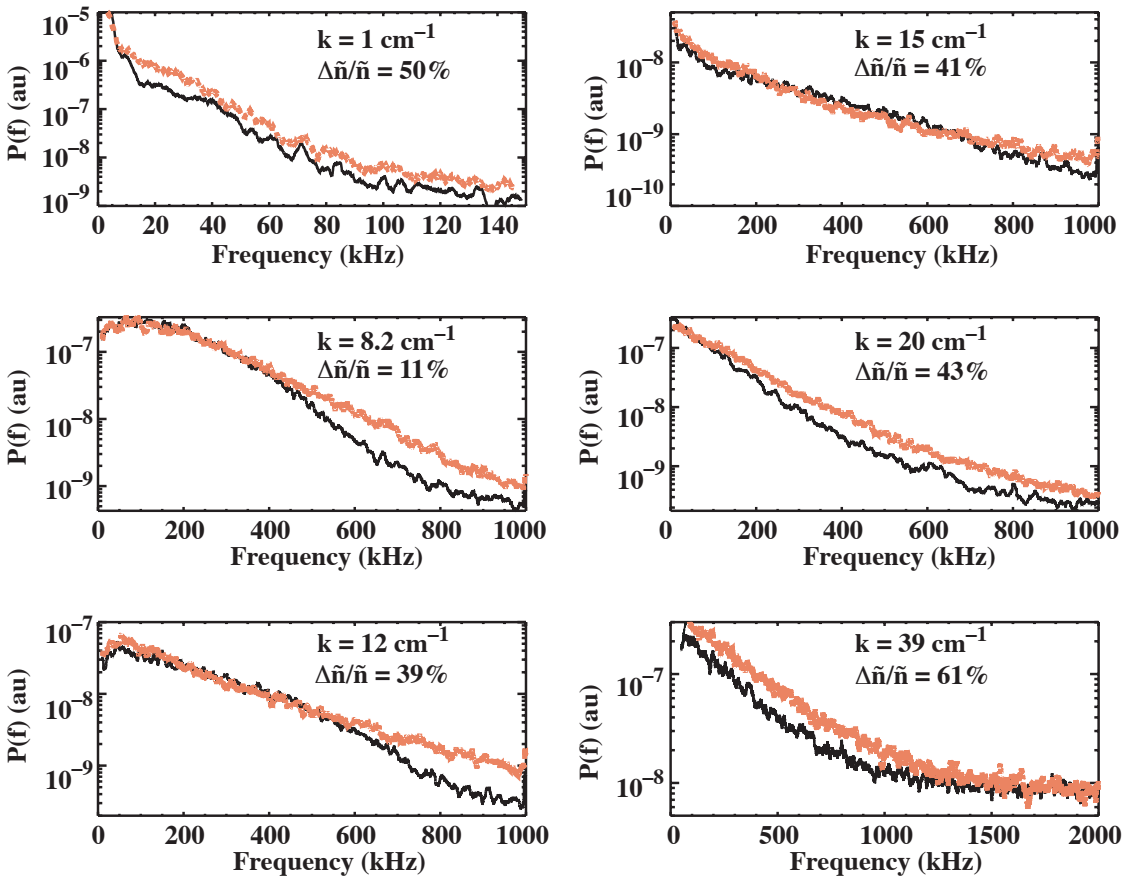

T.L. Rhodes Figure 5

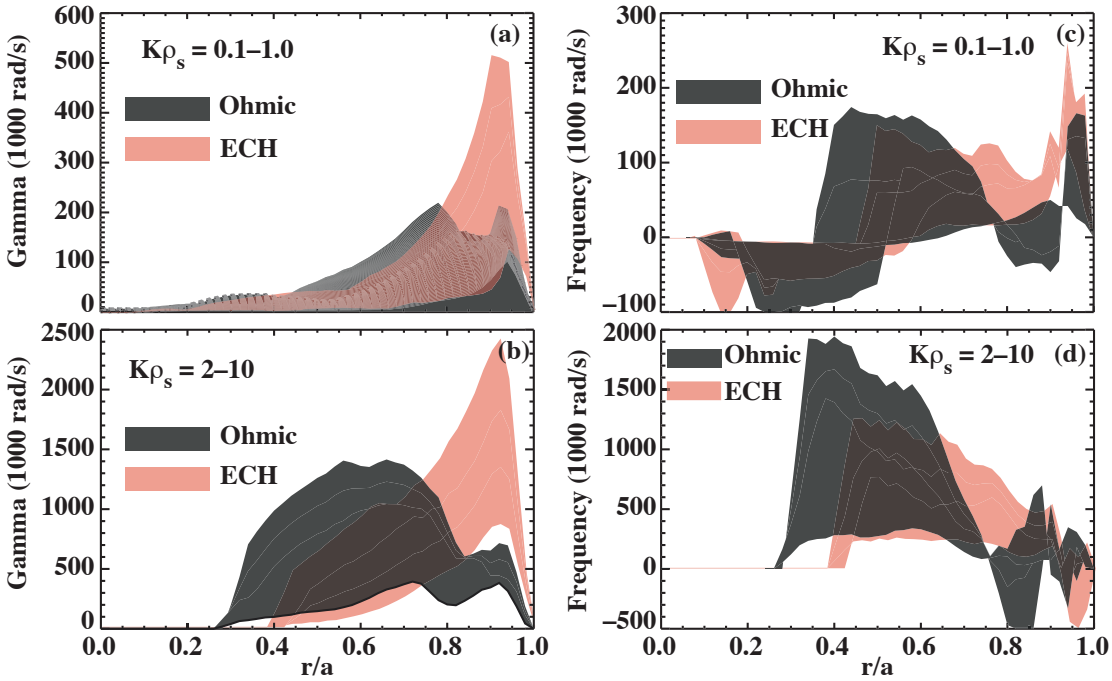

T.L. Rhodes Figure 6